

# Numerical Investigation on Molten Pool Dynamics During Multi-laser Array Powder Bed Fusion Process



LIU CAO

Multi-laser powder bed fusion (MLPBF) has become the most promising technology for rapid manufacturing of large metal parts. As a branch of MLPBF, multi-laser array powder bed fusion (MLA-PBF) has gradually attracted the attention of the industry, because of its advantages such as significantly speeding up production efficiency and low technical implementation difficulty. However, there is currently a lack of simulation studies based on the mesoscopic scale to describe the dynamic behavior of the MLA-PBF molten pool. The MLA-PBF spreading powder process was calculated herein based on the open source DEM framework Yade, the MLA-PBF molten pool dynamics was described based on the open source CFD framework OpenFOAM, and a multi-laser heat source model for real-time tracking of changes in the metal-phase and gas-phase interface was proposed. Aiming at the single-line mode of MLA-PBF, it was found that the dual-laser forming with low-front and high-rear could be used to preheat and pre-sinter the metal particles that were about to enter the molten pool, which was beneficial to reduce the pore defect in the solidified track, and a moderate laser beam space should be used. Aiming at the multi-line mode of MLA-PBF, it could form a molten pool with a significantly larger width and length than in the case of a single-laser beam, which was beneficial to eliminate pore defect in the formed zone, obtain a flat solidified track surface, and improve forming efficiency. When the laser power was low or the laser beam space was large, a large number of pores were prone to appear in the formed zone. As the laser power increased or the laser beam space decreased, when the laser energy was sufficient to melt the metal particles located in the lower part of the powder bed, a smooth surface of the solidified track and fewer pore defect would be obtained. This paper is expected to provide theoretical support for deepening the application of MLA-PBF in metal additive manufacturing.

<https://doi.org/10.1007/s11661-020-06076-6>

© The Minerals, Metals & Materials Society and ASM International 2020

## I. INTRODUCTION

LASER powder bed fusion (LPBF) is one of the most rapidly developing metal additive manufacturing technologies since the 21st century,<sup>[1]</sup> and has been directly used in the production of key parts in small batches in aerospace, biomedical and other fields.<sup>[2]</sup> However, because LPBF equipment generally uses a single-beam laser forming the powder bed, the so-called single-laser powder bed fusion (SLPBF), the forming efficiency and forming size are greatly restricted.<sup>[3,4]</sup> In view of this, multi-laser powder bed fusion (MLPBF) has gradually gained attention in recent years, and it has become one of the most promising technologies for rapid manufacturing of large metal parts.<sup>[5,6]</sup>

MLPBF technology is mainly divided into two categories: multi-laser forming area powder bed fusion<sup>[7]</sup> (MLFA-PBF) and multi-laser array powder bed fusion<sup>[8]</sup> (MLA-PBF). Among them, MLFA-PBF technology divides the powder bed into multiple forming zones, and then uses multiple laser beams to act on their respective forming zones simultaneously. Compared with the SLPBF process (Figure 1(a)), MLFA-PBF is equivalent to reducing the area of the forming zone for a single-laser beam (Figure 1(b)). MLFA-PBF generally uses two or four laser beams and uses fiber lasers.<sup>[9]</sup> MLA-PBF technology puts multiple laser beams side by side, and then acts on the powder bed at the same scanning speed. Compared with the SLPBF process, MLA-PBF is equivalent to widening the width of the laser action area (Figure 1(c)), or increasing the number of laser beams acting on a single solidified track (Figure 1(d)). MLA-PBF does not limit the number of laser beams (the number of laser beams in Reference [10] has reached sixteen), and the laser can be a diode laser<sup>[10]</sup> or a fiber laser.<sup>[11]</sup> The current MLPBF experimental researches mainly focus on the surface

Liu Cao is with the School of Mechanical and Electrical Engineering, Guangzhou University, Guangzhou, 510006 China  
Contact e-mail: caoliu@gzhu.edu.cn

Manuscript submitted August 31, 2020; accepted October 18, 2020.  
Article published online November 9, 2020

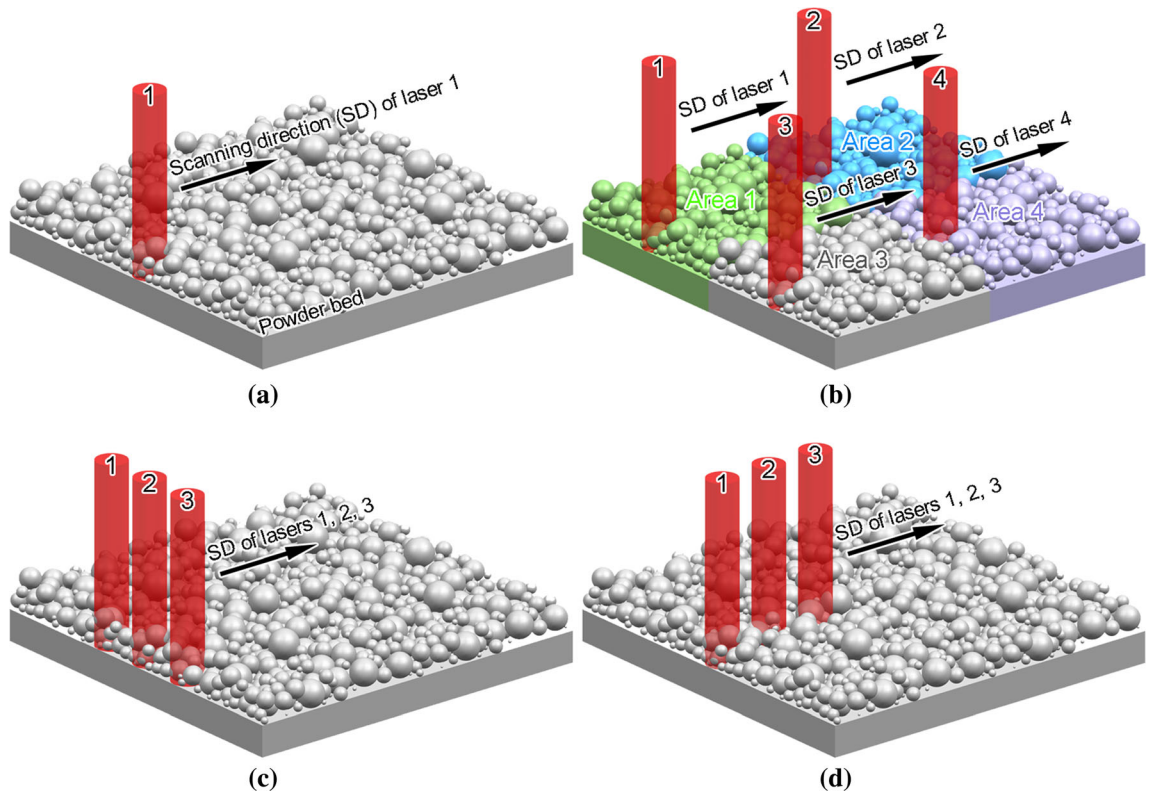


Fig. 1—Schematic diagram of LPBF process: (a) SLPBF; (b) MLFA-PBF; (c) MLA-PBF (the laser beam arrangement direction is perpendicular to the scanning direction); (d) MLA-PBF (the laser beam arrangement direction is parallel to the scanning direction).

roughness, porosity and microhardness of the parts.<sup>[12–14]</sup> Tsai *et al.*<sup>11</sup> used galvanometric scanner technology and a diffractive optical element to build an experimental MLA-PBF system, and the system has three-laser beams and the laser beam space could be adjusted. The experimental results showed that the three-laser beam method could reduce the surface roughness  $R_a$  to 3.2  $\mu\text{m}$  and the scanning time to 38.1 pct of the SLPBF process. Existing experimental research results<sup>[7–14]</sup> have provided great help for in-depth understanding of the MLPBF process.

The MLPBF process involves the synchronization between multiple laser beams and the powder bed, which is in a high temperature and rapidly changing environment. Numerical simulation technology can provide means to obtain three-dimensional and accurate LPBF process information,<sup>[15]</sup> such as the formation and elimination of pore defect.<sup>[16]</sup> At present, numerical simulation researches mainly focus on the SLPBF process, and the research factors mainly include spreading powder parameters (spreading powder method,<sup>[17]</sup> spreading powder speed,<sup>[18]</sup> particle size distribution,<sup>[19]</sup> spreading powder thickness,<sup>[20]</sup> etc.), laser parameters (laser power,<sup>[21]</sup> exposure time,<sup>[22]</sup> etc.) and scanning parameters (scanning speed,<sup>[23]</sup> hatch space,<sup>[24]</sup> etc.), and the purpose is to predict defects<sup>[25]</sup> such as pore and ball, and establish a reasonable SLPBF process map.<sup>[26]</sup> The current numerical simulation research for the MLPBF process is still in its infancy, mainly predicting the temperature<sup>[27]</sup> and stress<sup>[28]</sup> fields of the MLPBF

process based on the macroscopic scale, to obtain information such as the size of the molten pool and the distribution of internal stress.<sup>[29–31]</sup> Heeling *et al.*<sup>32</sup> predicted the size of the molten pool under different laser beam synchronization strategies for the dual-laser beam powder bed fusion process, and analyzed the porosity and dimensional deviation data obtained from the experiment. He found that compared to the SLPBF process, the use of dual-laser beams acting on a single solidified track could obtain more dense parts under certain conditions. Existing MLPBF simulation studies<sup>[27–32]</sup> do not directly describe the interaction of laser and metal particles on the mesoscopic scale, so it is impossible to accurately predict the molten pool dynamics in the MLPBF process. Especially for the MLA-PBF process, the molten pool dynamics when multiple laser beams act side by side on the powder bed has an important influence on the optimization of the MLA-PBF process, which is also the focus of this paper.

In this paper, the MLA-PBF spreading powder process was calculated based on the open source DEM framework Yade, and the dynamic behavior of the MLA-PBF molten pool was described based on the open source CFD framework OpenFOAM. For the single-line mode of MLA-PBF (multiple laser beams forming the same solidified track, Figure 1(d)) and the multi-line mode of MLA-PBF (multiple laser beams simultaneously forming multiple solidified tracks, Figure 1(c)), the influences of laser power and laser beam space on the forming process were simulated and

verified by comparison with experimental results. This paper is expected to provide theoretical support for deepening the application of MLA-PBF in metal additive manufacturing.

## II. MATHEMATICAL MODEL AND NUMERICAL SOLUTION

### A. Particle Dynamics Model

The premise of describing the molten pool dynamics in the MLA-PBF process based on the mesoscopic scale is to obtain the particle distribution of the powder bed. In the spreading powder process, the metal particles are pushed and squeezed by the roller, so a corresponding particle dynamic model needs to be established to describe the mechanical action between the roller and the particles, as well as the particles and the particles. The MLA-PBF spreading powder process was calculated herein based on the open source discrete element method (DEM) framework Yade,<sup>[17]</sup> which used DEM to describe the dynamic behavior of particles. Figure 2 shows the calculation flow of the spreading powder process, the main steps are: (a) a particle size distribution was artificially set, and an initial particle cluster satisfying the particle size distribution was generated in a certain space above the substrate; (b) the particle cluster was loosely spread on the substrate under the action of gravity; (c) the roller moved to spread powder; (d) after spreading powder, the sphere center coordinates and radius values of the particles above the substrate were derived, and the data were imported into the 3D modeling software to obtain the geometric model of the powder bed. The material parameters used include density ( $7270 \text{ kg/m}^3$ ), contact friction angle (0.1), Young's modulus ( $1.95 \times 10^{11} \text{ Pa}$ ) and Poisson's ratio (0.3).

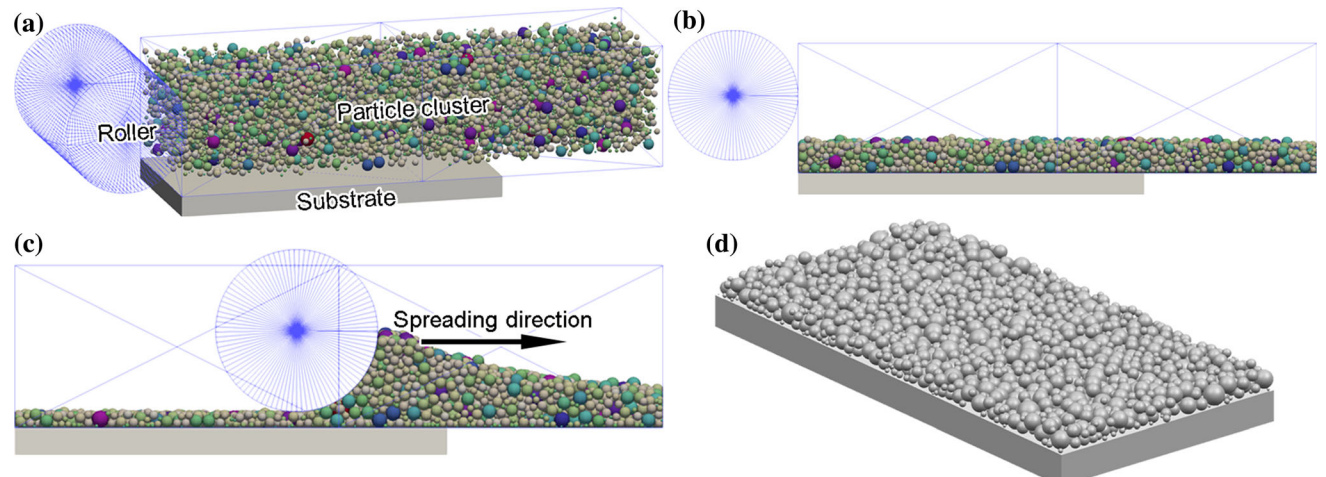


Fig. 2—Calculation flow of the spreading powder process: (a) generating particle cluster; (b) particle cluster falling; (c) roller spreading powder; (d) geometric model of powder bed.

### B. Molten Pool Dynamics Model

Equations [1] through [18] are the MLA-PBF molten pool dynamics model established herein, among which Eqs. [1] and [2] is the VOF model,<sup>[33]</sup> used to record the distribution of metal-phase and gas-phase; Eq. [3] is the momentum conservation equation, which considers the influences of pressure (Equation [6]), viscous force (Eq. [7]), gravity (Eq. [8]), drag force of the mushy zone (Eq. [9]), surface tension (Eq. [10]), Marangoni effect (Eq. [11]), and gasification recoil force (Eq. [12]) on the flow behavior of the molten pool; Eq. [4] is the energy conservation equation, which considers the influences of convection heat dissipation (Eq. [13]), radiation heat dissipation (Eq. [14]) and gasification heat dissipation (Eq. [15]) on the temperature of the molten pool; Eq. [5] is the mass conservation equation. In order to ensure the efficiency of numerical calculations, the following two assumptions were made: the flow behaviors of liquid metal and gas were regarded as laminar flow of incompressible Newtonian fluid, and the mass loss caused by metal gasification was not considered.

$$\frac{\partial \alpha_1}{\partial t} + \nabla \cdot (\alpha_1 \bar{u}) = 0 \quad [1]$$

$$\alpha_1 + \alpha_2 = 1 \quad [2]$$

$$\begin{aligned} \frac{\partial \bar{\rho} \bar{u}}{\partial t} + \nabla \cdot (\bar{\rho} \bar{u} \otimes \bar{u}) &= \vec{F}_{pressure} + \vec{F}_{viscous} + \vec{F}_{gravity} + \vec{F}_{mushy} \\ &+ (\vec{F}_{tension} + \vec{F}_{Marangoni} + \vec{F}_{recoil}) |\nabla \alpha_1| \frac{2\bar{\rho}}{\rho_1 + \rho_2} \end{aligned} \quad [3]$$

$$\begin{aligned} \frac{\partial \bar{\rho} \bar{c}_e T}{\partial t} + \nabla \cdot (\bar{\rho} \bar{u} \bar{c}_e T) - \nabla \cdot (\bar{k} \nabla T) &= -(q_{con} + q_{rad} + q_{gas}) |\nabla \alpha_1| \frac{2\bar{\rho} \bar{c}_e}{\rho_1 c_1 + \rho_2 c_2} + Q_{laser} \end{aligned} \quad [4]$$

$$\nabla \cdot \vec{u} = 0$$

[5]

$$\vec{F}_{gravity} = \bar{\rho} \vec{g}$$

[8]

$$\vec{F}_{pressure} = -\nabla p$$

[6]

$$\vec{F}_{mushy} = -\bar{\rho} K_C \left[ \frac{(1-f_{liquid})^2}{f_{liquid}^3 + C_K} \right] \vec{u}$$

[9]

$$\vec{F}_{viscous} = \nabla \cdot \left\{ 2\bar{\mu} \left[ \left( \frac{1}{2} \nabla \vec{u} + \frac{1}{2} (\nabla \vec{u})^T \right) - \frac{1}{3} (\nabla \cdot \vec{u}) \mathbf{I} \right] \right\}$$

[7]

$$\vec{F}_{tension} = \sigma \kappa \vec{n}$$

[10]

$$\vec{F}_{Marangoni} = \frac{d\sigma}{dT} [\nabla T - \vec{n}(\vec{n} \cdot \nabla T)]$$

[11]

$$\vec{F}_{recoil} = 0.54 P_0 \exp \left[ \frac{L_v m}{k_B} \left( \frac{1}{T_v} - \frac{1}{T} \right) \right] \vec{n}$$

[12]

$$q_{con} = h_{con}(T - T_{con})$$

[13]

$$q_{rad} = \sigma_s \varepsilon (T^4 - T_{rad}^4)$$

[14]

$$q_{gas} = 0.82 \frac{L_v m}{\sqrt{2\pi m k_B T}} P_0 \exp \left[ \frac{L_v m}{k_B} \left( \frac{1}{T_v} - \frac{1}{T} \right) \right]$$

[15]

$$\bar{\rho} = \alpha_1 \rho_1 + \alpha_2 \rho_2$$

[16]

$$\vec{n} = \frac{\nabla \alpha_1}{|\nabla \alpha_1|}$$

[17]

$$\kappa = -\nabla \cdot \vec{n}$$

[18]

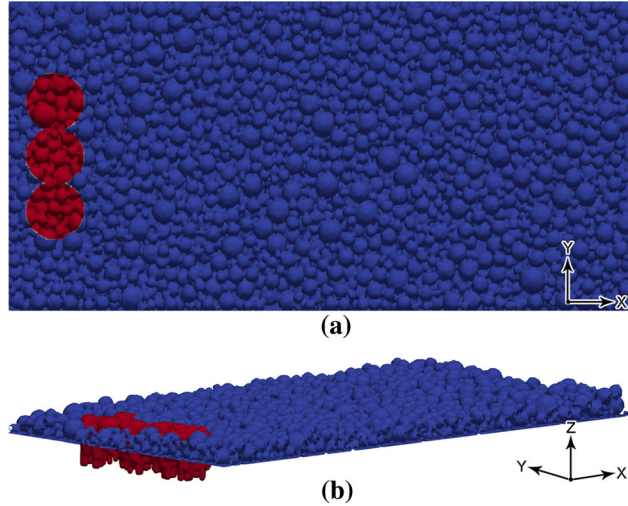
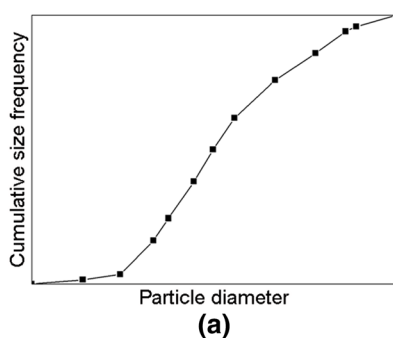
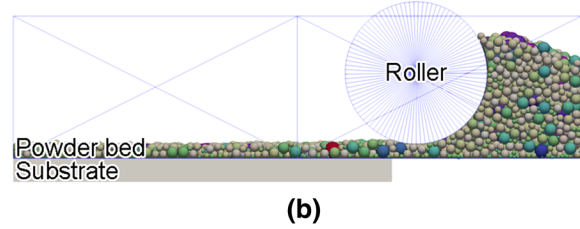


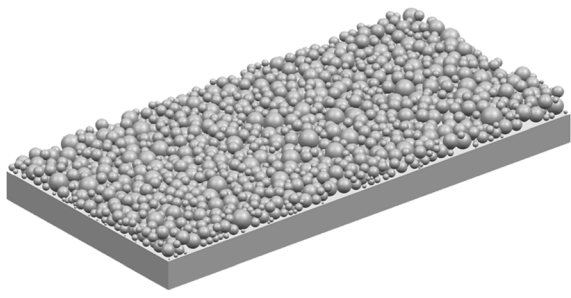
Fig. 3—Finding the laser action elements: (a) the elements directly acted by the laser (red area); (b) the laser action elements (red area) (Color figure online).



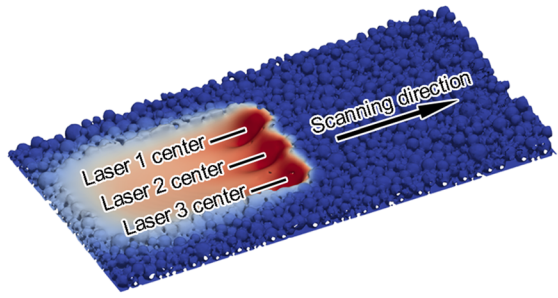
(a)



(b)



(c)



(d)

Fig. 4—MLA-PBF simulation process: (a) particle size distribution curve; (b) simulation of spreading powder; (c) geometric model of powder bed; (d) prediction of molten pool dynamic behavior.

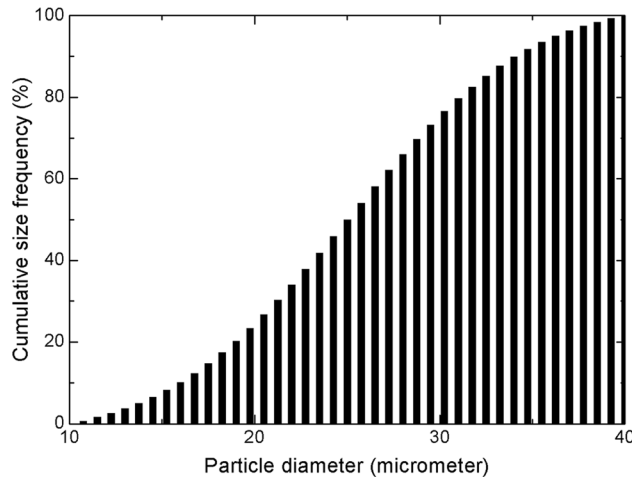


Fig. 5—Cumulative probability curve of particle size.

where  $\alpha_1$ ,  $\alpha_2$  are the volume fractions of the metal-phase and the gas-phase in the element, respectively;  $t$  is the time;  $\bar{u}$  is the velocity;  $\bar{\rho}$ ,  $\rho_1$ ,  $\rho_2$  are the mixed, metal-phase, and gas-phase densities, respectively;  $T$  is the temperature;  $\bar{c}_e$ ,  $c_1$ ,  $c_2$  are the equivalent,<sup>[20]</sup> metal-phase, and gas-phase specific heat capacities, respectively;  $\bar{k}$  is the mixed thermal conductivity;  $Q_{laser}$  is the laser energy density;  $p$  is the pressure;  $\bar{\mu}$  is the mixed dynamic viscosity;  $\mathbf{I}$  is the unit matrix;  $\bar{g}$  is the gravitational acceleration;  $K_C$  is the drag coefficient of mushy zone<sup>[34]</sup>;  $f_{liquid}$  is the liquid-phase fraction;  $C_K$  is a custom small value, such as  $1e-6$ ;  $\sigma$  is the surface tension coefficient;  $\kappa$  is the interface curvature;  $\bar{n}$  is the unit normal vector on the interface;  $\frac{d\sigma}{dT}$  is the rate of change of  $\sigma$  with temperature;  $P_0$  is the standard atmospheric pressure;  $L_v$  is the gasification latent heat of the metal;  $m$  is the molecular mass of the metal;  $k_B$  is the Boltzmann constant;  $T_v$  is the gasification temperature of the metal;  $h_{con}$  is the convective heat transfer coefficient on the interface;  $T_{con}$  is the external convection temperature;  $\sigma_s$  is the Stefan–Boltzmann constant;  $\varepsilon$  is the emissivity;  $T_{rad}$  is the external radiation temperature.

### C. Multi-laser Heat Source Model

Equations [19] and [20] is the multi-laser heat source model used in this paper. The steps of applying multi-laser energy are: (a) based on the horizontal coordinate ( $x_0$ ,  $y_0$ ) of the spot center, the spot radius  $R$  and the distribution of  $\alpha_1$ , the metal-phase elements directly acting on multi-laser beams were found (Figure 3(a)); (b) taking the elements obtained in Step (a) as starting points, the elements within a certain distance along the direction of gravity were marked, and these elements were the laser action elements (Figure 3(b)); (c) according to the coordinates of the center point of the laser action element (such as the body center of a cube), the laser action elements whose horizontal coordinates were close to overlap were

regarded as a group, and the laser energy in this area was considered to be absorbed by this group of elements; (d) the laser energy percentage  $f_{\Delta z}$  occupied by each laser action element was determined by the metal-phase volume fraction of the element, for example, the  $\alpha_1$  value of a certain laser action element  $m$  is 0.5, a certain element group  $M$  searched in Step (c) contains element  $m$ , and the sum of the  $\alpha_1$  values of group  $M$  is 10, then the  $f_{\Delta z}$  value of element  $m$  is 5 pct.

$$Q_{laser} = \frac{f_{\Delta z} q_{laser}}{\Delta z} \quad [19]$$

$$q_{laser} = \frac{2\eta P_{laser}}{\pi R^2} \exp\left(-2 \frac{(x - x_0 - vt)^2 + (y - y_0)^2}{R^2}\right) \quad [20]$$

where  $f_{\Delta z}$  is the laser energy percentage;  $\Delta z$  is the element equivalent size, such as the side length of the cube;  $q_{laser}$  is the surface energy density of the laser;  $\eta$  is the laser absorption rate of the metal;  $P_{laser}$  is the laser power;  $R$  is the radius of the laser spot;  $x$ ,  $y$  are the horizontal coordinates of the center point of the element;  $x_0$ ,  $y_0$  are the horizontal coordinates of the center point of the laser spot;  $v$  is the scanning speed of the laser.

### D. Simulation Process for MLA-PBF

Figure 4 shows the MLA-PBF simulation process, which mainly includes four steps: (a) with the aid of experimental means (such as particle size analyzer) or literature data, the particle size distribution curve was obtained; (b) regarding the morphology of metal particles as an ideal sphere, the spreading powder process was predicted based on the open source DEM framework Yade, and the sphere center coordinates and radius values of the particles were derived; (c) with the aid of 3D modeling software, the geometric model of the powder bed was obtained; and (d) based on the open source computational fluid dynamics (CFD) framework OpenFOAM,<sup>[20,21,24,25]</sup> the dynamic behavior of MLA-PBF molten pool was described.

## III. RESULTS AND DISCUSSION

### A. Calculation Parameters

The alloy material used herein is 316L stainless steel, and its chemical composition (mass percentage) is: Fe 65.395 pct-Cr 17.0 pct-Ni 12.0 pct-Mo 2.5 pct-Mn 2.0 pct-Si 1.0 pct-P 0.045 pct-C 0.03 pct-S 0.03 pct. The particle size distribution used in the spreading powder process satisfied the Gaussian distribution, with a center value of 25  $\mu\text{m}$  and a variance of 7.5  $\mu\text{m}$ , and the particle diameter was artificially controlled within the range of 10 to 40  $\mu\text{m}$ . Figure 5 shows the cumulative probability curve of the particle size herein.

**Table I. Physical Property Parameters of 316L Stainless Steel**

Parameter	Value	Unit
Density of Metal	7270	kg/m <sup>3</sup>
Specific Heat of Metal	790	J/(kg·K)
Thermal Conductivity of Metal	24.55	W/(m·K)
Solidus Temperature	1658	K
Liquidus Temperature	1723	K
Evaporation Temperature	3090	K
Latent Heat of Melting	$2.7 \times 10^5$	J/kg
Latent Heat of Gasification	$7.45 \times 10^6$	J/kg
Viscosity of Liquid Metal	0.00345	Pa·s
Surface Tension	1.6	N/m
Temperature of Surface Tension	$-8 \times 10^{-4}$	N/(m·K)
Molecular Mass	$9.3 \times 10^{-26}$	kg
Ambient Pressure	101325	Pa
Boltzmann Constant	$1.380649 \times 10^{-23}$	J/K
Emissivity	0.26	
Stefan–Boltzmann constant	$5.67 \times 10^{-8}$	W/(m <sup>2</sup> ·K <sup>4</sup> )
Density of Air	1	kg/m <sup>3</sup>
Specific Heat of Air	718	J/(kg·K)
Thermal Conductivity of Air	0.02346	W/(m·K)
Viscosity of Air	$1.48 \times 10^{-5}$	Pa·s

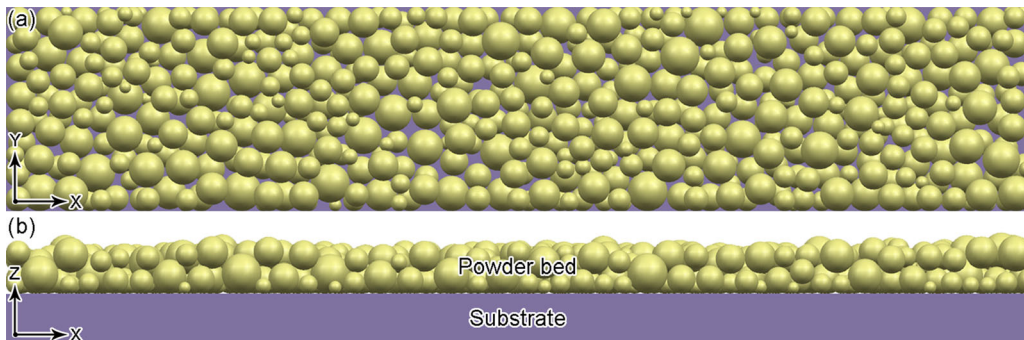


Fig. 6—Particle distribution in single-line mode: (a) top view; (b) side view.

**Table II. Calculation Schemes in Single-Line Mode**

Calculation Scheme	Number of Laser Beam	Laser Power (W)	Scanning Speed (m/s)	Laser beam Space ( $\mu\text{m}$ )	Initial Phase Distribution
s1	1	200	1.5	none	particle distribution shown in Figure 6
s2	1	50	1.5	none	particle distribution shown in Figure 6
s3	1	200	1.5	none	final phase distribution of scheme s2
s4	2	200/50	1.5	52.5	particle distribution shown in Figure 6
s5	2	50/200	1.5	17.5	particle distribution shown in Figure 6
s6	2	50/200	1.5	35	particle distribution shown in Figure 6
s7	2	50/200	1.5	52.5	particle distribution shown in Figure 6
s8	2	50/200	1.5	70	particle distribution shown in Figure 6
s9	2	50/200	1.5	87.5	particle distribution shown in Figure 6

(In the table, the laser beam space is the space between the centers of adjacent laser beams in the X-direction.).

The physical property parameters of 316L stainless steel required to predict the MLA-PBF process based on OpenFOAM are shown in Table I. The computing resource configuration used was Intel Xeon Gold 5120 CPU (dual CPU, 56 threads, and 96 GB memory).

### B. Simulation Studies of Single-Line Mode

The single-line mode was first focused, that is, considering the situation where multiple laser beams form the same solidified track (Figure 1(d)). Figure 6 shows the particle distribution of the powder bed in the

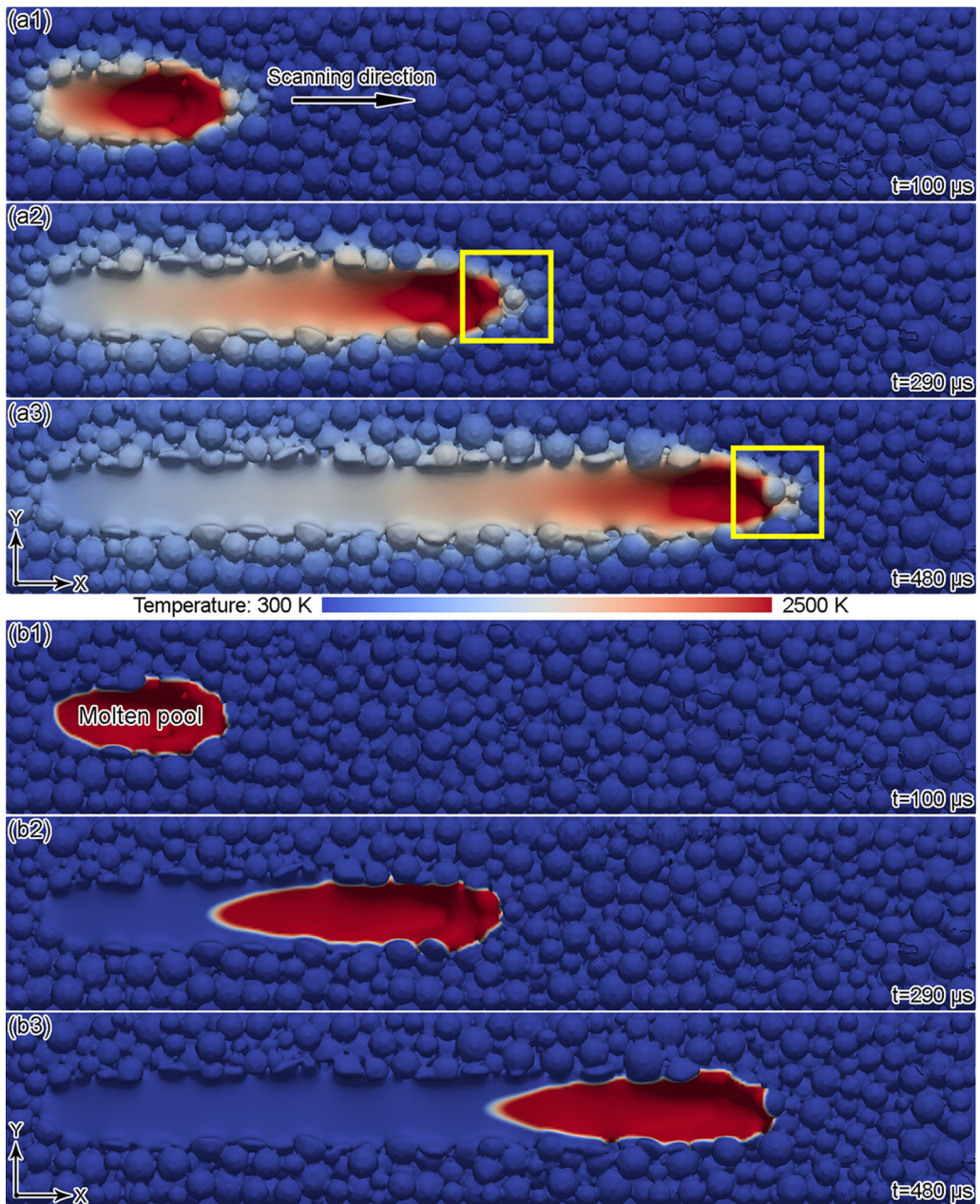


Fig. 7—Simulation result of calculation scheme s7: (a1 to a3) temperature distribution at different times; (b1 to b3) molten pool morphology at different times (red indicates liquid-phase, blue indicates solid-phase) (Color figure online).

single-line mode, where the geometric dimensions of the substrate are:  $X$ -direction (1000  $\mu\text{m}$ ),  $Y$ -direction (200  $\mu\text{m}$ ), and  $Z$ -direction (50  $\mu\text{m}$ ), and the thickness of the powder bed is 45  $\mu\text{m}$ . The geometric dimensions of the mesh model are:  $X$ -direction (1000  $\mu\text{m}$ ),  $Y$ -direction (200  $\mu\text{m}$ ) and  $Z$ -direction (145  $\mu\text{m}$ ), and the mesh size is 2.5  $\mu\text{m}$ . Table II shows the calculation schemes in the single-line mode, where the laser beam moved from the horizontal coordinate (50, 100  $\mu\text{m}$ ) to the horizontal coordinate (950, 100  $\mu\text{m}$ ). When the number of laser beams is 2, the laser power “200 W/50 W” means that the power of the front-laser beam is 200 W and the power of the rear-laser beam is 50 W when viewed along the scanning direction. In addition, the laser spot radius

was 35  $\mu\text{m}$ , the initial temperature of all calculation schemes was 300 K, and the time step used in the calculation was 2.5e-7 s.

To illustrate the difference between dual-laser forming and single-laser forming, here is a comparative analysis of calculation schemes s1, s3, and s7. Among them, schemes s1 and s3 used a single-laser beam, and scheme s7 used dual-laser beams. The difference between schemes s1 and s3 is that the initial phase distribution of scheme s1 was the particle distribution shown in Figure 6, while the initial phase distribution of scheme s3 is the final phase distribution of scheme s2. Figure 7 is the simulation result of calculation scheme s7. The metal particles were gradually melted

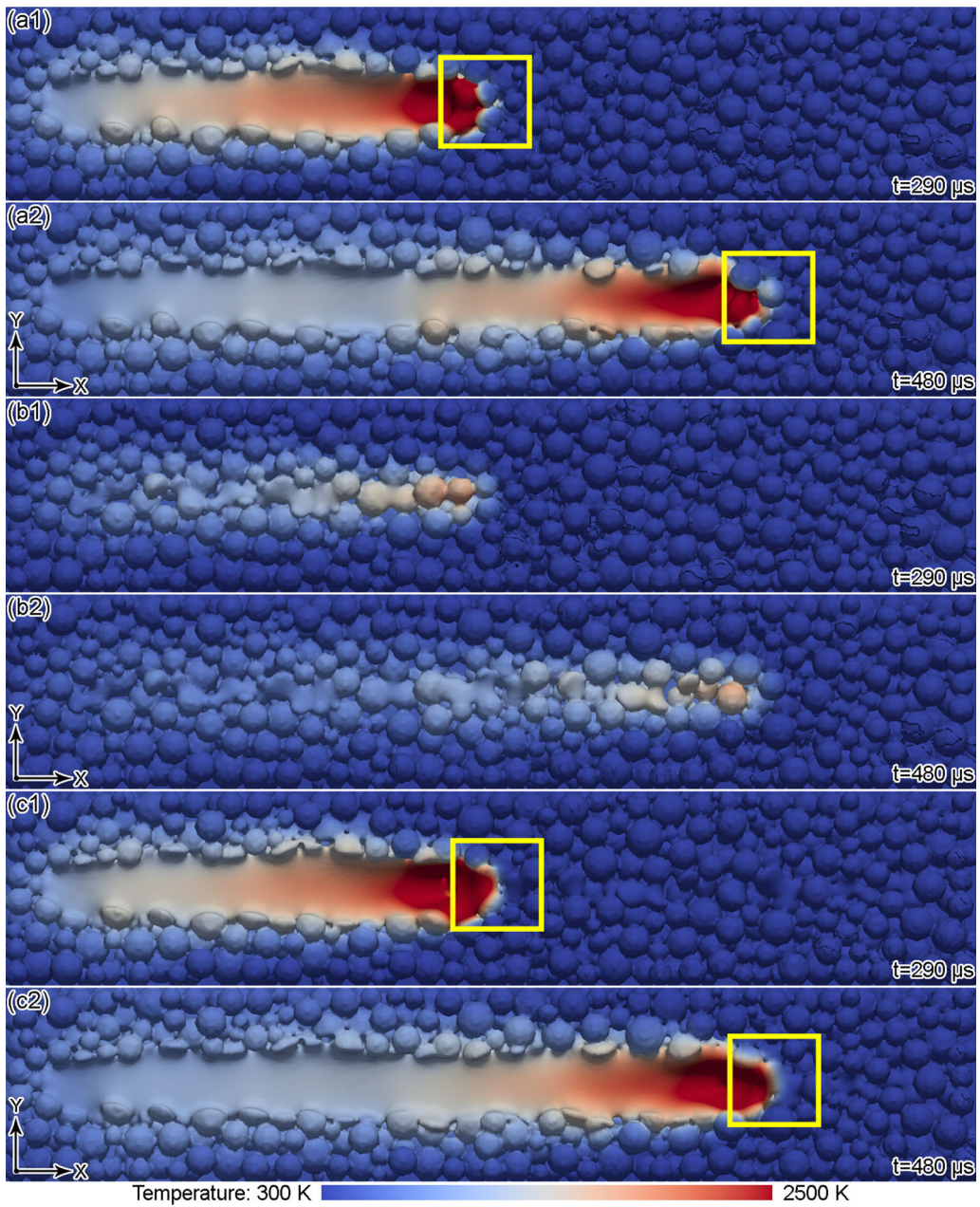


Fig. 8—Temperature distribution under different calculation schemes: (a1, a2) scheme s1; (b1, b2) scheme s2; (c1, c2) scheme s3.

by laser heating to form a molten pool, and then cool down and solidify into a solidified track. Figure 8 shows the temperature distribution at different times under calculation schemes s1 to s3. Comparing the yellow box area in Figures 7a2, 8(a1) and (c1), it can be found that the temperature of the particles in front of the molten pool in calculation scheme s7 was significantly higher than that of schemes s1 and s3, and the same phenomenon can also be found by comparing Figures 7(a3), 8(a2), and (c2). The reason is obvious. In calculation scheme s7, the power of the front-laser beam was 50 W and the power of the rear-laser beam was 200 W. Most of the metal particles were heated by the higher-energy rear-laser beam to form a molten pool, and the front-laser beam with lower energy could

only increase the temperature of the metal particles or partially melt them. Figure 9 shows the laser action areas at a certain time under calculation schemes s1, s3 and s7. The comparison result better proves that the front-laser beam in calculation scheme s7 mainly acted in front of the molten pool. Comparing calculation schemes s1 and s7, it can be found that the front-laser beam in scheme s7 preheated the metal particles that were about to enter the molten pool on the one hand, and played a role of pre-sintering on the other hand. Comparing calculation schemes s3 and s7, it can be found that the front-laser beam in scheme s7 mainly played a preheating role.

Figure 10 shows the final pore defect distribution of calculation schemes s1, s3 and s7, and the non-red spots

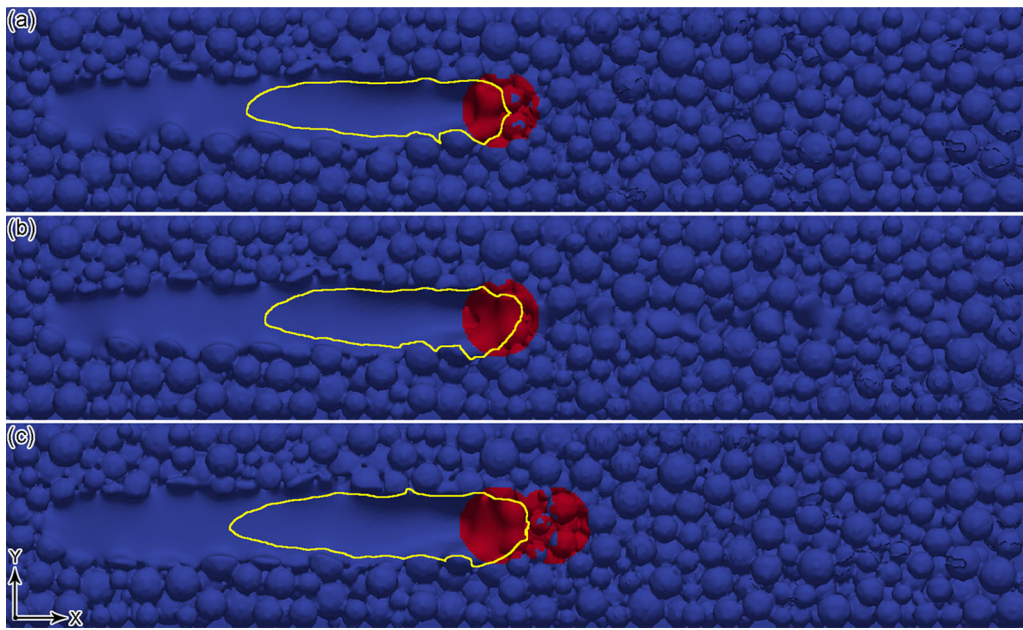


Fig. 9—Laser action area at  $290 \mu\text{s}$  under different calculation schemes (red indicates the laser action area, yellow indicates the molten pool boundary): (a) scheme s1; (b) scheme s3; (c) scheme s7 (Color figure online).

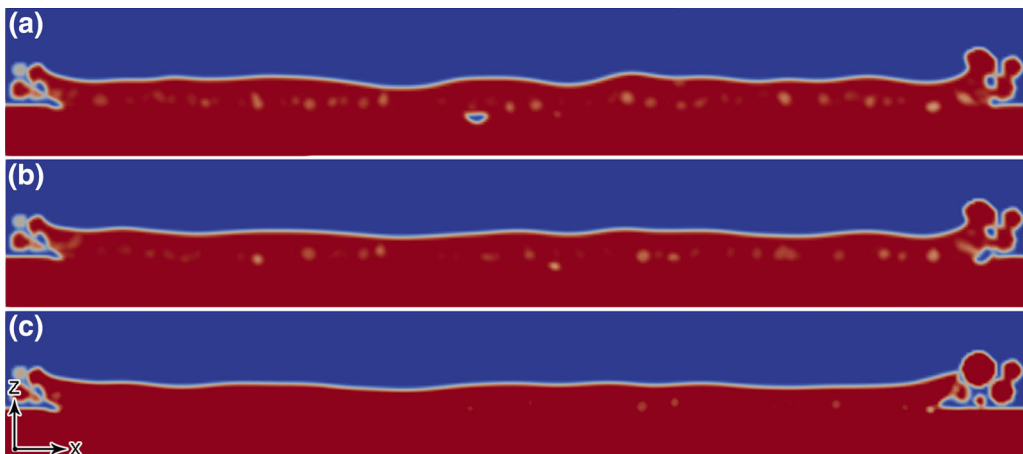


Fig. 10—Final pore distribution in  $Y$ -direction middle section under different calculation schemes (red indicates metal-phase, blue indicates gas-phase): (a) scheme s1; (b) scheme s3; (c) scheme s7 (Color figure online).

contained in the red metal-phase in the figure were the locations of the pores (the volume fraction of the metal-phase was not 100 pct). It can be seen from the comparison result that the pore defect of scheme s3 was less than that of scheme s1. The reason is that scheme s3 was pre-sintered before forming, which was equivalent to reducing the thermal resistance between metal particles in advance, so that the powder bed could better absorb the laser energy during the forming process. Scheme s7 has fewer pore defect than scheme s3. The reason is that the front-laser beam in scheme s7 played a preheating function, that is, increased the overall temperature of the molten pool, which was beneficial to exhaust the gas involved in the molten pool. It can be seen that compared with the single-laser forming, the dual-laser forming (low-power front-laser beam and

high-power rear-laser beam) can preheat and pre-sinter the metal particles that are about to enter the molten pool, which is beneficial to reduce pore defect in the solidified track.

To illustrate the difference between the front-laser power and the rear-laser power being high or low, calculation schemes s4 and s7 were compared and analyzed, among which scheme s4 was front-high and rear-low, and scheme s7 was front-low and rear-high. Figure 11 shows the temperature and pore distribution of calculation schemes s4 and s7. Comparing the yellow box areas in Figure 11(a) and (b), it can be seen that because the front-laser beam of scheme s4 had higher power, the molten pool in scheme s4 was more forward than that in scheme s7 at the same time (along the positive  $X$ -direction). Since the rear-laser beam with

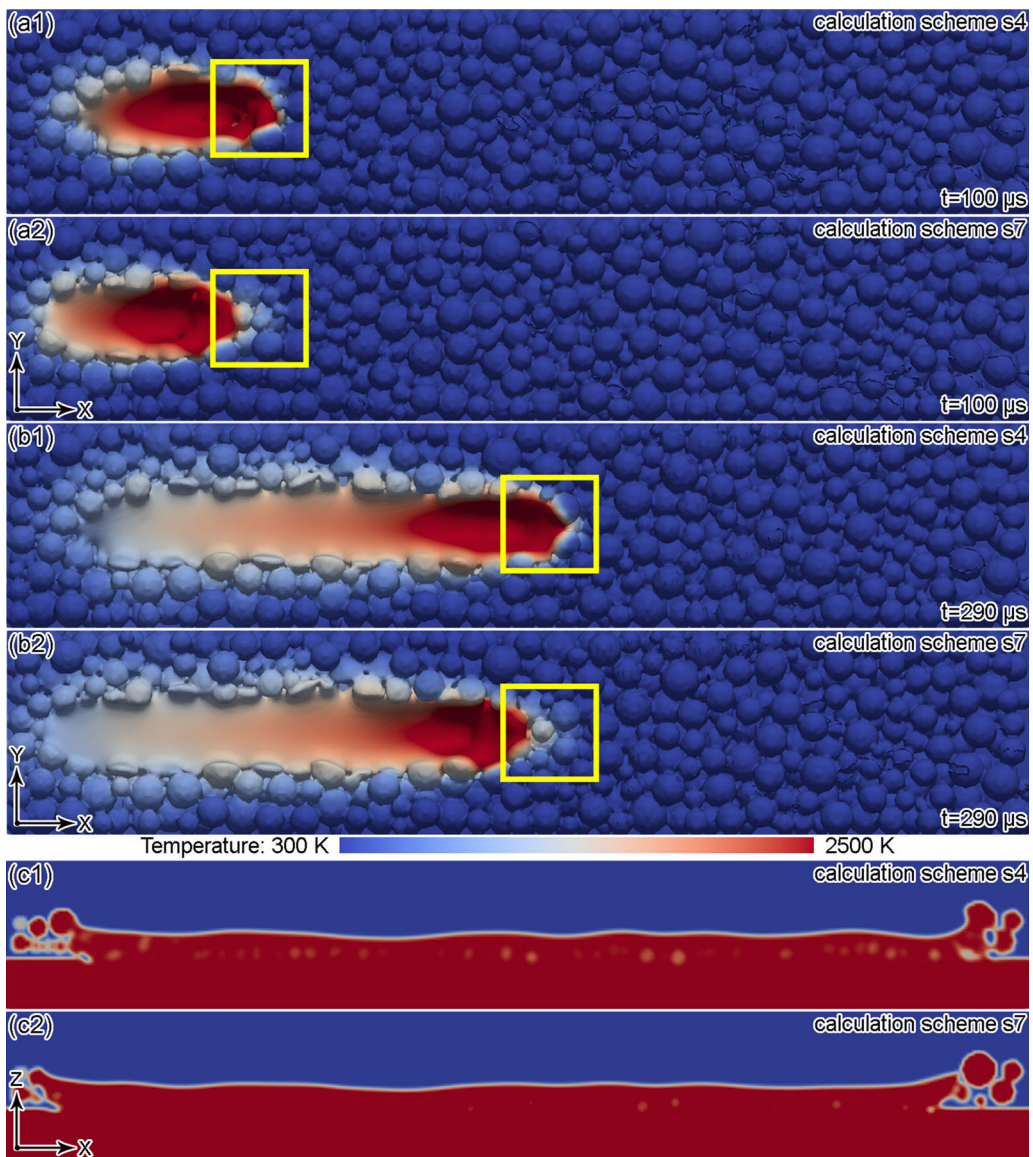


Fig. 11—Simulation results of calculation scheme s4 and s7: (a1, a2) temperature distribution at  $100 \mu\text{s}$ ; (b1, b2) temperature distribution at  $290 \mu\text{s}$ ; (c1, c2) pore distribution.

lower power in scheme s4 directly acted on the molten pool, the metal particles in front of the molten pool in scheme s4 could not be preheated and pre-sintered. From the pore distribution in Figure 11(c), it can be found that the pore defect of scheme s7 was significantly less than that of scheme s4. The reason is that the dual-laser forming with high-front and low-rear could not be used to preheat and pre-sinter the metal particles that were about to enter the molten pool. It can be seen that from the perspective of reducing pore defect, the dual-laser forming with low-front and high-rear is better than the dual-laser forming with high-front and low-rear.

In order to study the influence of the laser beam space on the dual-laser forming process with low-front and high-rear, calculation schemes s5 to s9 were compared and analyzed. Figure 12 shows the pore distribution of calculation schemes s5 to s9. From the comparison

results, it can be found that as the space between the laser beams gradually increased, the pore defect in the solidified track first decreased and then increased, and the same conclusion could be drawn from the experimental data in Reference.<sup>[32]</sup> The reason is that when the laser beam space was too small, the action areas of the front-laser beam and the rear-laser beam mostly overlapped, so that the laser energy applied to the particles in front of the molten pool was limited, and it was difficult to perform effective preheating and pre-sintering. When the laser beam space was too large, the metal particles in a certain position were preheated and pre-sintered under the action of the front-laser beam; however, because the time required for the rear-laser beam to reach this position was too long, the metal-phase temperature in front of the molten pool was not high, causing the front-laser beam to lose its preheating function. It can be seen that a moderate laser

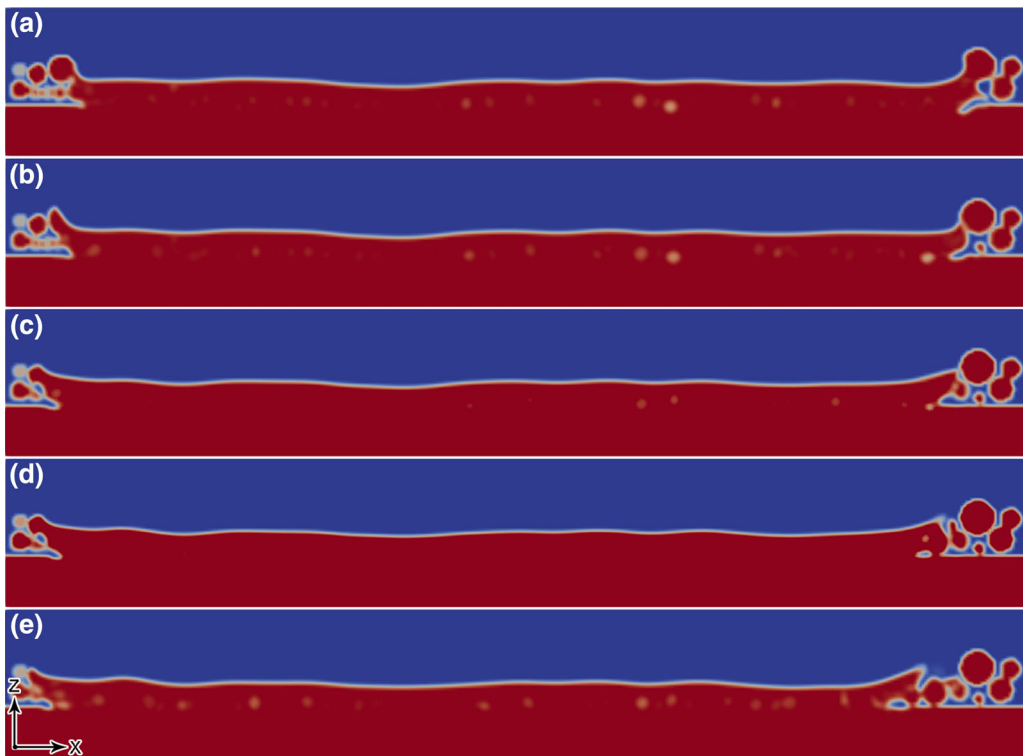


Fig. 12—Pore distribution under different calculation schemes: (a) scheme s5; (b) scheme s6; (c) scheme s7; (d) scheme s8; (e) scheme s9.

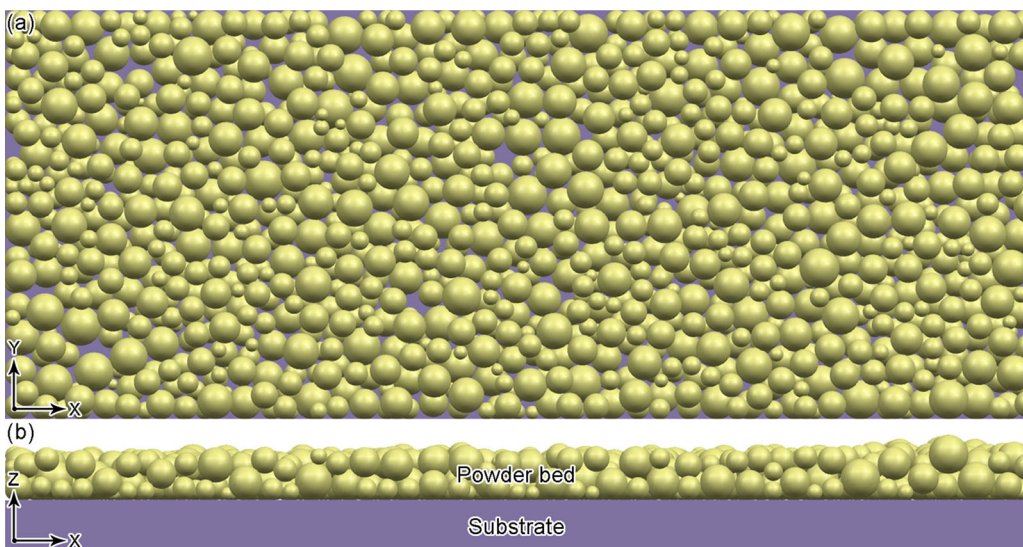


Fig. 13—Particle distribution in multi-line mode: (a) top view; (b) side view.

beam space should be used for the dual-laser forming of low-front and high-rear. The optimal laser beam space obtained herein is the value of the spot diameter.

### C. Simulation Studies of Multi-line Mode

The multi-line mode was then focused, that is, considering the situation where multiple laser beams simultaneously form multiple solidified tracks (Figure 1(c)). Figure 13 shows the particle distribution

of the powder bed in the multi-line mode, where the geometric dimensions of the substrate are as follows:  $X$ -direction (1000  $\mu\text{m}$ ),  $Y$ -direction (400  $\mu\text{m}$ ), and  $Z$ -direction (50  $\mu\text{m}$ ), and the thickness of the powder bed is 45  $\mu\text{m}$ . The geometric dimensions of the mesh model are as follows:  $X$ -direction (1000  $\mu\text{m}$ ),  $Y$ -direction (400  $\mu\text{m}$ ), and  $Z$ -direction (145  $\mu\text{m}$ ), and the mesh size is 2.5  $\mu\text{m}$ . Table III shows the calculation schemes in the multi-line mode, where the laser beams all moved from the  $X$ -coordinate of 50  $\mu\text{m}$  to the  $X$ -coordinate of 950

Table III. Calculation Schemes in Multi-line Mode

Calculation Scheme	Number of Laser Beam	Laser Power (W)	Scanning Speed (m/s)	Laser Beam Space ( $\mu\text{m}$ )	Initial Phase Distribution
m1	1	200	1	none	particle distribution shown in Figure 13
m2	1	200	1	none	final phase distribution of scheme m1
m3	1	200	1	none	final phase distribution of scheme m2
m4	3	160	1	60	particle distribution shown in Figure 13
m5	3	180	1	60	particle distribution shown in Figure 13
m6	3	200	1	60	particle distribution shown in Figure 13
m7	3	220	1	60	particle distribution shown in Figure 13
m8	3	200	1	70	particle distribution shown in Figure 13
m9	3	200	1	80	particle distribution shown in Figure 13

In the table, the laser power represents the power of a single-laser beam, and the laser beam space is the space between the centers of adjacent laser beams in the  $Y$ -direction.

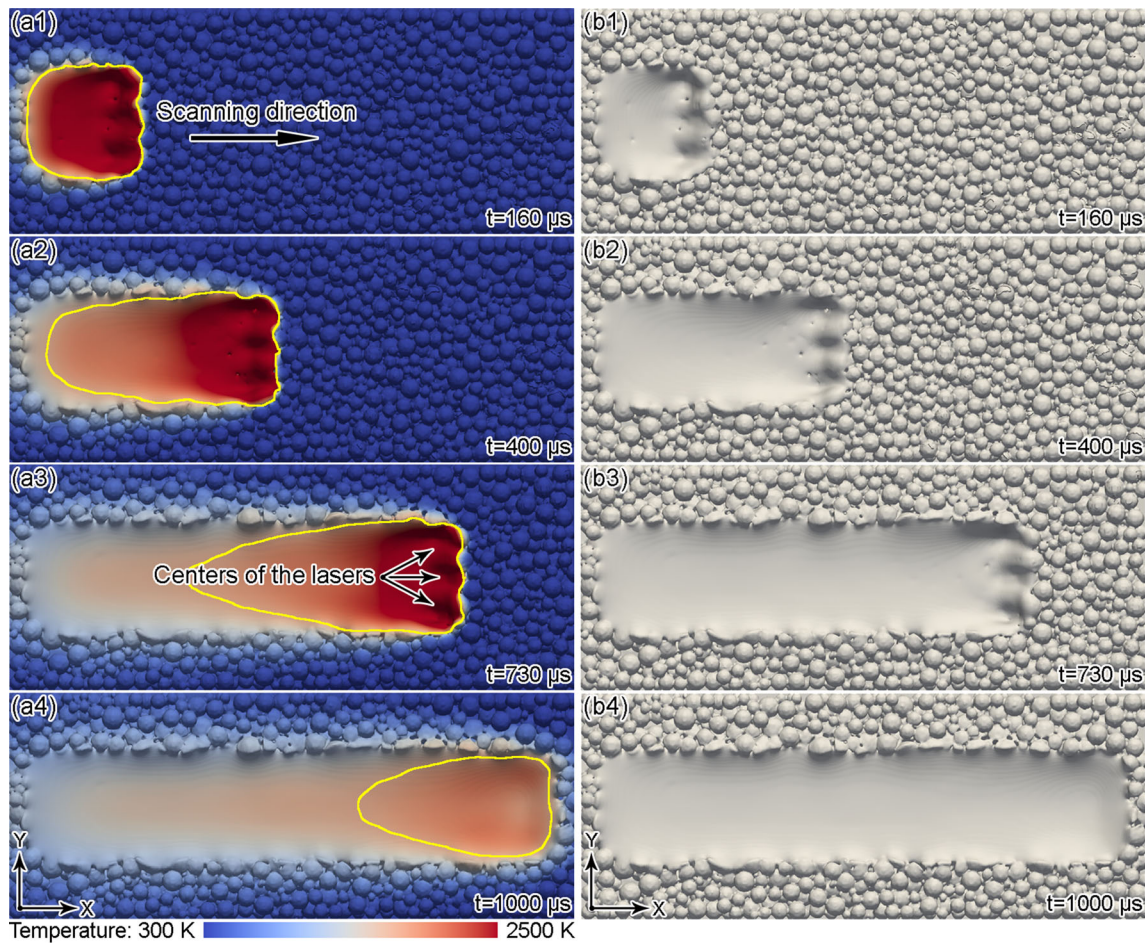


Fig. 14—Simulation results of calculation scheme m6 (parts 1 to 4 represent different times): (a) temperature distribution at different times (yellow curve represents the boundary of the molten pool); (b) solidified track morphology at different times (Color figure online).

$\mu\text{m}$ . In addition, the laser spot radius was  $35 \mu\text{m}$ , the initial temperature of all calculation schemes was  $300 \text{ K}$ , and the time step used in the calculation was  $2.5e-7 \text{ s}$ . It should be noted that in addition to the different initial phase distributions, the  $Y$ -axis coordinates of the laser beam center in calculation schemes m1 to m3 were also different, which were  $140 \mu\text{m}$ ,  $200 \mu\text{m}$ , and  $260 \mu\text{m}$ , respectively.

Figure 14 shows the simulation results of calculation scheme m6. In this scheme, three side-by-side laser beams were used. Compared with the forming process in the single-line mode (Figure 7), the width and length of the molten pool were significantly larger at this time, thereby obtaining a wider solidified track. To illustrate the difference between multi-line mode and single-laser forming, calculation schemes m1 to m3 were divided

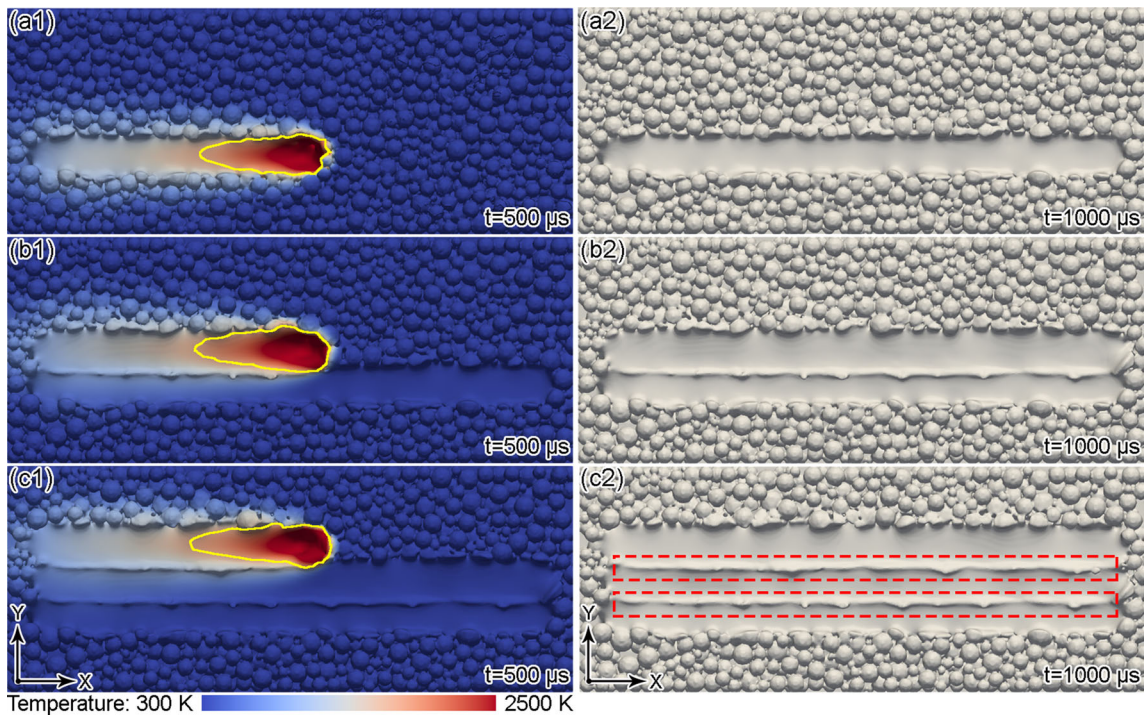


Fig. 15—Temperature distribution at intermediate time (yellow curve represents the boundary of the molten pool, *a*1 to *c*1) and final solidified track morphology (*a*2, *b*2, and *c*2) under calculation schemes m1 to m3: (a) scheme m1; (b) scheme m2; (c) scheme m3 (Color figure online).

into three single-laser forming to obtain the same laser action area as scheme m6. Figure 15 shows the simulation results of schemes m1 to m3. Since the initial temperatures of the solidified track and the powder bed in calculation schemes m2 and m3 were both 300 K, under the influence of Marangoni effect, there were obvious bumps between the solidified tracks in scheme m3 (the red dashed frame area in Figure 15(*c*2)), and the solidified track surface in scheme m6 was flat. On the other hand, because the energy of a single-laser beam presents a typical two-dimensional Gaussian distribution in the horizontal plane, the laser energy absorbed by the region between the solidified tracks in calculation schemes m1 to m3 was less, and it was easy to form pore defect between the solidified tracks. By extracting the metal-phase and gas-phase interface of the final simulation results, Figure 16 shows the pore distribution in the formed zone under calculation schemes m3 and m6. From the bottom view (Figure 16(*a*1)) and side view (Figure 16(*b*1)) of the pore distribution under calculation scheme m3, it can be seen that a large number of pore appeared between the solidified tracks and near the substrate (the red dashed frame area in Figure 15(*a*1) and (*b*1)), while the inside of the formed zone under scheme m6 contained only a small amount of pore (Figure 16(*a*2) and (*b*2)). In summary, compared with single-laser forming, the width and length of the molten pool in the multi-line mode are significantly larger, which is beneficial to eliminate pore defect, obtain a smooth surface of the solidified track, and improve forming efficiency.

In order to analyze the influence of laser power on the multi-line mode, different laser powers were set in calculation schemes m4 to m7. Figure 17 shows the simulation results of the solidified track morphology and pore defect in schemes m4 to m7. It can be seen from the comparison results that with the increase of laser power, the solidified track surface has been kept flat (Figure 17(*a*1) to (*a*4)), while the pore defect inside the formed zone gradually reduced (Figure 17(*b*1) to (*b*4) and (*c*1) to (*c*4)), and the relatively suitable laser power was 200 W. The reason is that the metal particles located in the upper part of the powder bed absorbed significantly more laser energy than the lower particles, so that even at lower laser power, the upper particles could be completely melted, thus obtaining a flat solidified track surface. For the particles in the lower part, when the laser power was low, the particles were difficult to melt completely, and the gas between the particles could not escape effectively, so a large number of pore were formed. In summary, when the laser power is low, a large number of pore are prone to appear in the formed zone. As the laser power increases, when the laser energy is sufficient to melt the metal particles located in the lower part of the powder bed, a smooth surface of the solidified track and fewer pore defect will be obtained.

In order to analyze the influence of laser beam space on the multi-line mode, different laser beam spaces were set in calculation schemes m6, m8, and m9. Figure 18 shows the simulation results of the solidified track morphology and pore defect in schemes m6, m8, and m9. It can be seen from the comparison results that with the increase of laser beam space, the solidified track

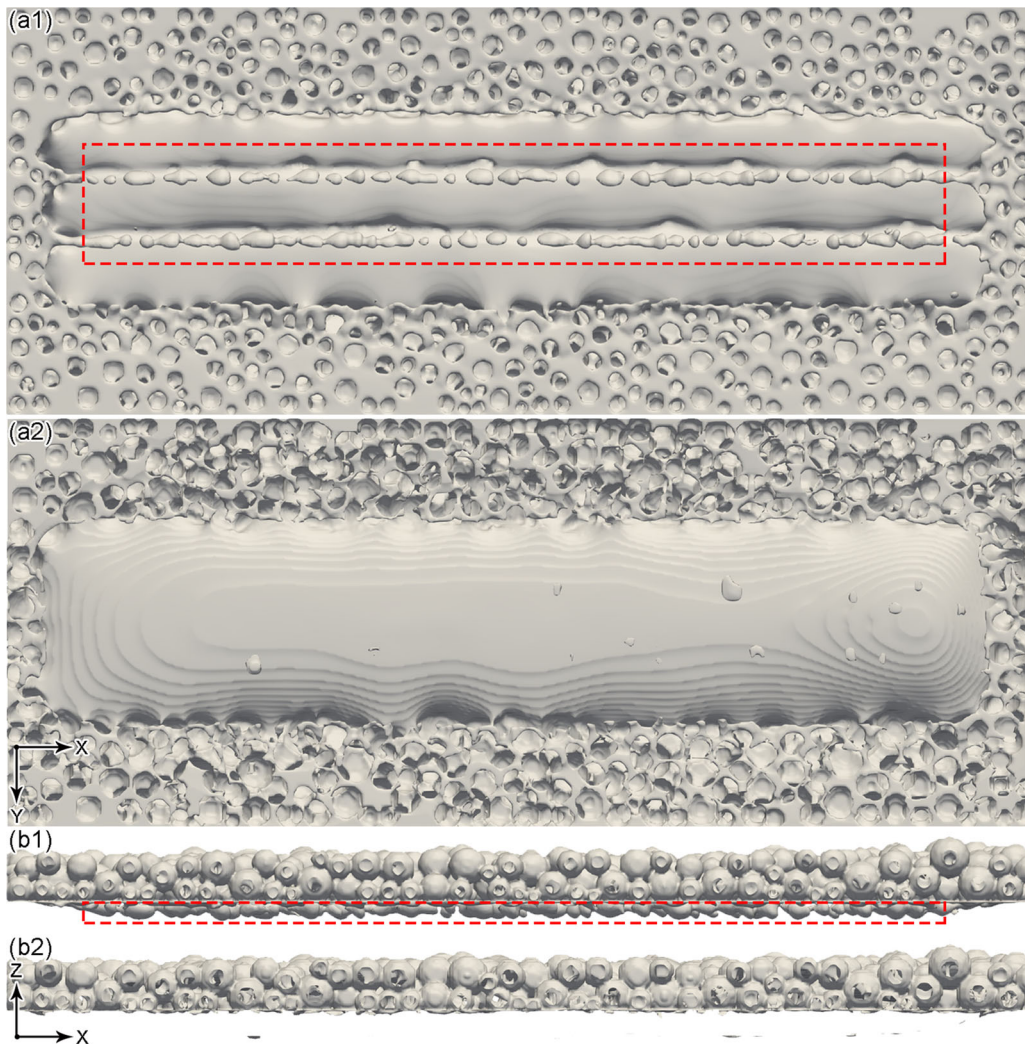


Fig. 16—Pore distribution in the formed zone under calculation scheme m3 and m6: (a1, b1) scheme m3; (a2, b2) scheme m6.

surface has been kept flat (Figure 18(a1) to (a3)), while the pore defect inside the formed zone gradually increased (Figure 18(b1) to (b3) and (c1) to (c3)), and the relatively suitable laser beam space was 60  $\mu\text{m}$ . The reason is that the metal particles located in the upper part of the powder bed absorbed significantly more laser energy than the lower particles, so that even at larger laser beam space, the upper particles could be completely melted, thus obtaining a flat solidified track surface. For the particles in the lower part, when the laser beam space was large, the particles were difficult to melt completely, and the gas between the particles could not escape effectively, so a large number of pores were formed. The same conclusion could be drawn from the experimental results in Reference.<sup>[11]</sup> In summary, when the laser beam space is large, a large number of pores are prone to appear in the formed zone. As the laser beam space reduces, when the laser energy is sufficient to melt the metal particles located in the lower part of the powder bed, a smooth surface of the solidified track and fewer pore defects will be obtained.

#### IV. CONCLUSIONS

- (1) The spreading powder process of multi-laser array powder bed fusion (MLA-PBF) was calculated based on the open source DEM framework Yade, the MLA-PBF molten pool dynamics was described based on the open source CFD framework OpenFOAM, and a multi-laser heat source model for real-time tracking of changes in the metal-phase and gas-phase interface was proposed.
- (2) Aiming at the single-line mode of MLA-PBF, it was found that the dual-laser forming with low-front and high-rear could be used to preheat and pre-sinter the metal particles that were about to enter the molten pool, which was beneficial to reduce the pore defect in the solidified track, and a moderate laser beam space should be used. The optimal laser beam space obtained herein was the value of the laser spot diameter.

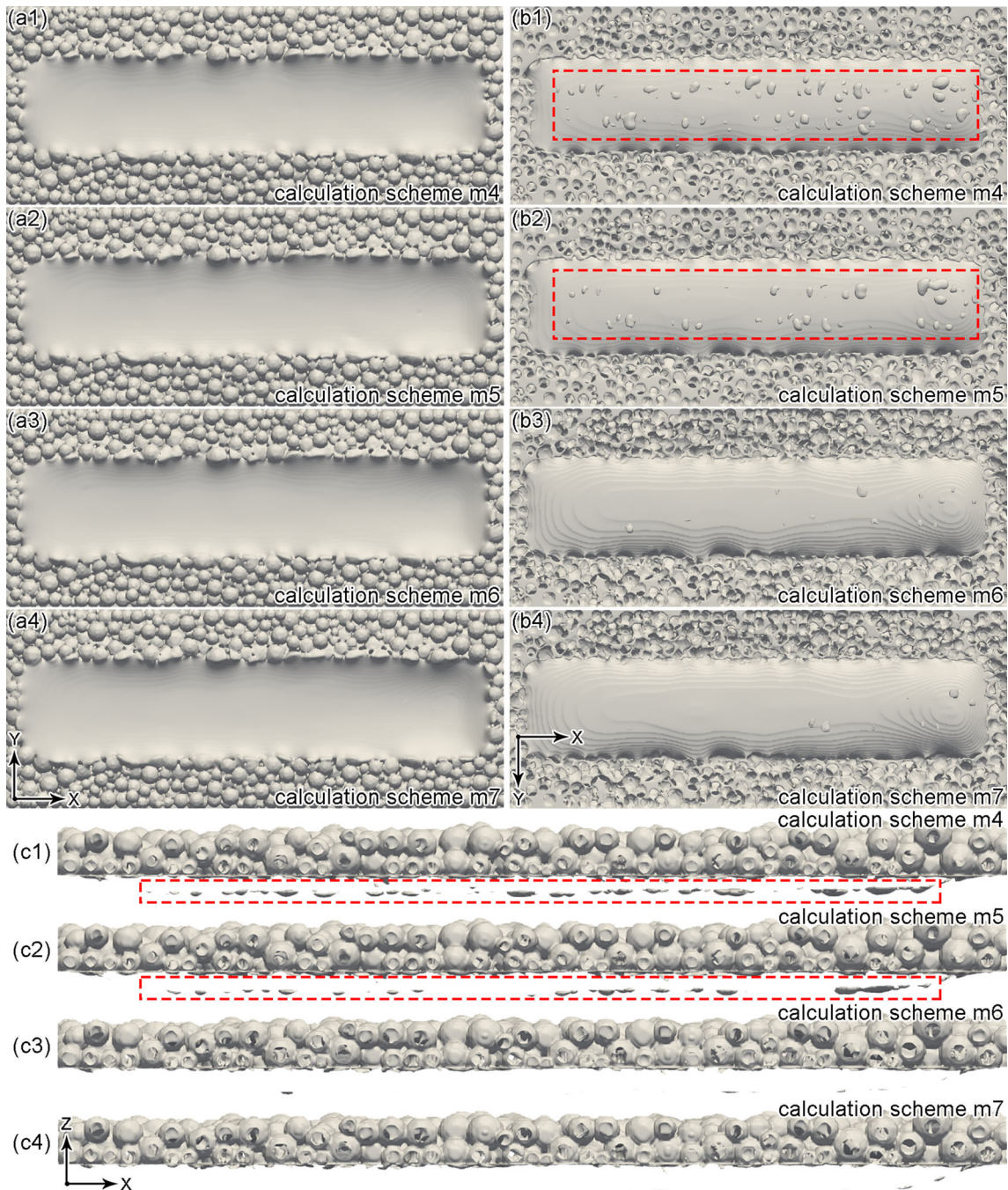


Fig. 17—Simulation results of solidified track morphology (a) and pore defect (b, c) in schemes m4 to m7: (a1 to c1) scheme m4; (a2 to c2) scheme m5; (a3 to c3) scheme m6; (a4 to c4) scheme m7.

(3) Aiming at the multi-line mode of MLA-PBF, it could form a molten pool with a significantly larger width and length than in the case of a single-laser beam, which was beneficial to eliminate pore defect in the formed zone, obtain a flat solidified track surface, and improve forming efficiency. When the laser power was low or the laser beam space was large, a large number of pores were prone to appear in the formed zone. As the laser power increased or the laser beam space decreased, when the laser energy was

sufficient to melt the metal particles located in the lower part of the powder bed, a smooth surface of the solidified track and fewer pore defect would be obtained. The optimal laser power and laser beam space obtained herein were 200 W and 60  $\mu\text{m}$ , respectively.

(4) The main focus of this paper is the pore defect during MLA-PBF process, and studies<sup>[35,36]</sup> have shown that the spatter evolution behavior is also one of the influencing factors that cannot be

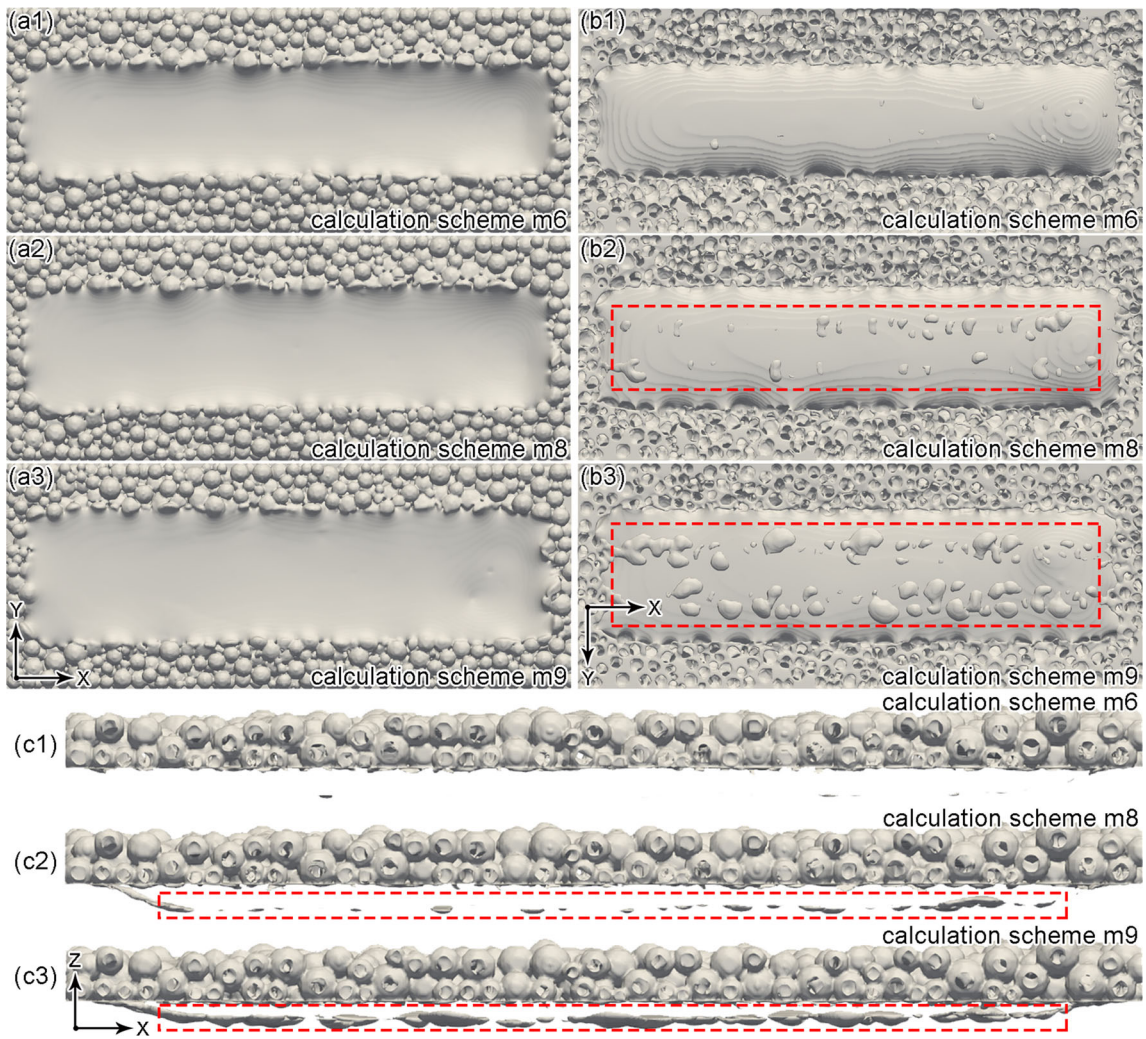


Fig. 18—Simulation results of solidified track morphology (a) and pore defect (b, c) in schemes m6, m8, and m9: (a1 to c1) scheme m6; (a2, to c2) scheme m8; (a3 to c3) scheme m9.

ignored in LPBF process, which is an important direction for subsequent research.

## ACKNOWLEDGMENTS

This work was supported by the Natural Science Foundation of Guangdong Province (No. 2019A1515012040).

## REFERENCES

1. A. Salmi, F. Calignano, M. Galati, and E. Atzeni: *Virtual Phys. Prototy.*, 2018, vol. 13 (3), pp. 191–202.
2. B. Fotovatni, N. Namdari, and A. Dehghanghadikolaei: *Mater. Res. Express*, 2019, vol. 6, p. 012002.
3. A. Khorasani, I. Gibson, J.K. Veetil, and A.H. Ghasemi: *Int. J. Adv. Manuf. Tech.*, 2020, vol. 108, pp. 191–209.
4. T. DebRoy, H.L. Wei, J.S. Zuback, T. Mukherjee, J.W. Elmer, J.O. Milewski, A.M. Beese, A. Wilson-Heid, A. De, and W. Zhang: *Prog. Mater. Sci.*, 2018, vol. 92, pp. 112–224.
5. P. Wagenblast, J. Risse, S. Schweikert, and J. Zaiss: *Proc. SPIE*, 2020, <https://doi.org/10.1117/12.2551154>.
6. F. Eibl, C. Tenbrock, T. Pichler, T. Schmithüschen, D. Heussen, J. H. Schleifenbaum: *Proceedings of the 2017 High Power Diode Lasers and Systems Conference*, 2017, <https://doi.org/10.1109/hpd.2017.8261078>.
7. S.F. Wen, C.Z. Yan, Q.S. Wei, L.C. Zhang, X. Zhao, W. Zhu, and Y.S. Shi: *Virtual Phys. Prototy.*, 2014, vol. 9 (4), pp. 213–23.
8. A. T. Payne: *Doctoral thesis*, 2017, England: University of Cambridge.
9. H. Wong, K. Dawson, G.A. Ravi, L. Howlett, R.O. Jones, and C.J. Sutcliffe: *Int. J. Adv. Manuf. Tech.*, 2019, vol. 105, pp. 2891–2906.
10. J. Karp, V. Ostroverkhov, D. Bogdan, M. Graham, B. McCarthy, and W. Carter: *Proc. SPIE*, 2019, <https://doi.org/10.1117/12.2513892>.
11. C.-Y. Tsai, C.-W. Cheng, A.-C. Lee, and M.-C. Tsai: *Addit. Manuf.*, 2019, vol. 27, pp. 1–7.
12. B. Liu, Z.Z. Kuai, Z.H. Li, J.B. Tong, P.K. Bai, B.Q. Li, and Y.F. Nie: *Materials*, 2018, vol. 11, p. 2354.
13. F.Z. Li, Z.M. Wang, and X.Y. Zeng: *Mater. Lett.*, 2017, vol. 199, pp. 79–83.
14. F. Eibl: *Doctoral thesis*, 2017, Germany: RWTH Aachen University.
15. S.A. Khairallah, A.T. Anderson, A. Rubenchik, and W.E. King: *Acta Mater.*, 2016, vol. 108, pp. 36–45.

16. K.Q. Le, C. Tang, and C.H. Wong: *Int. J. Therm. Sci.*, 2019, vol. 145, p. 105992.
17. L. Cao: *Int. J. Adv. Manuf. Tech.*, 2019, vol. 105, pp. 2253–69.
18. E.J.R. Parteli and T. Pöschel: *Powder Technol.*, 2016, vol. 288, pp. 96–102.
19. D.D. Gu, M.J. Xia, and D.H. Dai: *Int. J. Mach. Tool. Manu.*, 2019, vol. 137, pp. 67–78.
20. L. Cao: *Int. J. Heat Mass Tran.*, 2019, vol. 141, pp. 1036–48.
21. C. Tang, J.L. Tan, and C.H. Wong: *Int. J. Heat Mass Tran.*, 2018, vol. 126, pp. 957–68.
22. M. Zheng, L. Wei, J. Chen, Q. Zhang, J.Q. Li, S. Sui, G. Wang, and W.D. Huang: *Appl. Surf. Sci.*, 2019, vol. 496, p. 143649.
23. C. Panwisawas, C.L. Qiu, M.J. Anderson, Y. Sovani, R.P. Turner, M.M. Attallah, J.W. Brooks, and H.C. Basoalto: *Comp. Mater. Sci.*, 2017, vol. 126, pp. 479–90.
24. L. Cao: *Metall. Mater. Trans. A*, 2020, vol. 51A, pp. 4130–45.
25. L. Cao: *Comp. Mater. Sci.*, 2020, vol. 179, p. 109686.
26. H. Kyogoku, T.-T. Ikeshoji: *Mech. Engineering Rev.*, 2020, vol. 7, no. 1, pp. 19-00182.
27. M. Zavala-Arredondo, H. Ali, K.M. Groom, and K. Mumtaz: *Int. J. Adv. Manuf. Tech.*, 2018, vol. 97, pp. 1383–96.
28. S. Zou, H.B. Xiao, F.P. Ye, Z.C. Li, W.Z. Tang, F. Zhu, C.T. Chen, and C. Zhu: *Results Phys.*, 2020, vol. 16, p. 103005.
29. C.P. Chen, Z.X. Xiao, H.H. Zhu, and X.Y. Zeng: *J. Mater. Process. Tech.*, 2020, vol. 284, p. 116726.
30. M. Masoomi, S.M. Thompson, and N. Shamsaei: *Manuf. Lett.*, 2017, vol. 13, pp. 15–20.
31. T. Heeling and K. Wegener: *Phys. Procedia*, 2016, vol. 83, pp. 899–908.
32. T. Heeling, L. Zimmermann, and K. Wegener: *Proceedings of Solid Freeform Fabrication Symposium*, 2016, <https://doi.org/10.3929/ethz-a-010803938>.
33. L. Cao, D.M. Liao, F. Sun, T. Chen, Z.H. Teng, and Y.L. Tang: *Int. J. Adv. Manuf. Technol.*, 2017, vol. 94, pp. 807–15.
34. L. Cao, F. Sun, T. Chen, Z.H. Teng, Y.L. Tang, and D.M. Liao: *Acta Metall. Sin.*, 2017, vol. 53 (11), pp. 1521–31.
35. S. A. Khairallah, A. A. Martin, J. R. I. Lee, G. Guss, N. P. Calta, J. A. Hammons, M. H. Nielsen, K. Chaput, E. Schwalbach, M. N. Shah, M. G. Chapman, T. M. Willey, A. M. Rubenchik, A. T. Anderson, Y. M. Wang, M. J. Matthews, W. E. King: *Science*, vol. 368, pp. 660–65.
36. Q.L. Guo, C. Zhao, L.I. Escano, Z. Young, L.H. Xiong, K. Fezaa, W. Everhart, B. Brown, T. Sun, and L.Y. Chen: *Acta Mater.*, 2018, vol. 151, pp. 169–80.

**Publisher's Note** Springer Nature remains neutral with regard to jurisdictional claims in published maps and institutional affiliations.